A large-stroke electrostatic micro-actuator

S Towfighian[1], A Seleim[2], E M Abdel-Rahman[3,4] and G R Heppler[3]

[1] Mechanical and Industrial Engineering, University of Toronto, Toronto, Ontario, Canada
[2] Industrial and Manufacturing Systems Engineering, University of Windsor, Ontario, Canada
[3] System Design Engineering, University of Waterloo, Waterloo, Ontario, Canada

E-mail: sherryt@mie.utoronto.ca, seleim@uwindsor.ca, eihab@uwaterloo.ca and heppler@uwaterloo.ca

Abstract

Voltage-driven parallel-plate electrostatic actuators suffer from an operation range limit of 30% of the electrostatic gap; this has restrained their application in microelectromechanical systems. In this paper, the travel range of an electrostatic actuator made of a micro-cantilever beam above a fixed electrode is extended quasi-statically to 90% of the capacitor gap by introducing a voltage regulator (controller) circuit designed for low-frequency actuation. The voltage regulator reduces the actuator input voltage, and therefore the electrostatic force, as the beam approaches the fixed electrode so that balance is maintained between the mechanical restoring force and the electrostatic force. The low-frequency actuator also shows evidence of high-order superharmonic resonances that are observed here for the first time in electrostatic actuators.

(Some figures in this article are in colour only in the electronic version)

1. Introduction

Extending the range of electrostatic actuation is desirable in many applications including microelectromechanical systems (MEMS) optical switches [1], tunable laser diodes [2], polychromator gratings [3], optical modulators [4] and millipede data storage systems [5]. To extend the travel range of electrostatic actuators in attracting mode beyond the conventional one-third of the capacitor gap, researchers have used various methods including charge and current control [6–9], and leveraged bending [10]. Other approaches that seek to extend the travel range of electrostatic actuators include voltage control [11–13], sliding mode control [14] and other nonlinear feedback controllers [15–17].

Charge and current control are very difficult to perform in MEMS because of the very small capacitance. Using a capacitor in series with the actuator to control the charge, Chan *et al* [9] experimentally increased travel up to 60% of the gap at the cost of high-voltage requirements. Adding a capacitor in series, they kept the electrostatic force constant in the actuator by controlling the voltage difference between the

actuator plates. As the gap decreases in the actuator beyond 30% of the gap, its capacitance increases rapidly, while the voltage across the actuator plates decreases as the square of the gap helping to keep the electrostatic force constant. Theoretically, it should have been possible to operate over the full gap of the actuator, but parasitic capacitance limited the travel range to 60% of the gap. Leveraged bending [10] is another method to increase the actuation range by applying the electrostatic force only to a portion of the actuator. The disadvantage of this method is high input voltage requirements.

Current control was examined by Guardia *et al* [8]. They used open-loop and closed-loop configurations for driving the actuator with a current source. They showed that full gap actuation is achievable with a voltage five times the open-loop pull-in voltage. Experimentally they obtained actuation up to 48% of the gap. The drawback of this method was that the actuator was stable only for a short period of time.

There are a number of studies using charge control for extending electrostatic actuation [6, 7]. Using a switched-capacitor circuit, Seeger *et al* [6] controlled the charge of an electrostatic actuator. They showed analytically that the

---

[4] Author to whom any correspondence should be addressed.

pull-in instability can be eliminated by taking advantage of parasitic capacitance present in the actuator and employing a voltage 5.2 times smaller than that of voltage-controlled systems. They experimentally achieved 83% of the gap. However, tip-in instability, which arises from a small rotation of the parallel-plate actuator, and snapping could not be eliminated using this technique.

Using voltage control, Chen *et al* [12] stabilized the tilt angle of an electrostatic micro-mirror beyond its snap-down angle. They controlled the actuation voltage, keeping the slope of the mechanical torque larger than the electrostatic torque to stabilize the angle of the mirror. They were able to extend the stable operation range to 10° from an open-loop pull-in angle of 6.1°. Simulation studies correlated well with experiments at low actuation angles; at large actuation angles, the linear mechanical and damping force models could not predict the overshoot accurately.

Employing a nonlinear voltage controller that uses two control methods, feedback linearization and trajectory planning, Agudelo *et al* [13] experimentally achieved actuation up to 60% of the gap, well beyond pull-in, for an electrostatic micro-mirror. They used feedback of the mirror tilt angle and the actuation voltage to follow the desired angle trajectory beyond pull-in and obtained good agreement with simulation. Simulation showed actuation over the whole gap; this was limited in practice by the sampling time which restricted the actuation to 60% of the gap.

A nonlinear output tracking controller was proposed by Owusu *et al* [16] to extend the electrostatic actuation range using displacement, velocity and charge feedback. Simulations showed robust response in the presence of noise and an increased actuation range to 90% of the gap. Further studies on this controller were conducted by Nikpanah *et al* [17] who improved the performance by eliminating the displacement fluctuations present in the previous study when using a switching control technique that made the controller more feasible to implement.

A closed-loop controller that used a capacitive sensor for position feedback was designed by Lu and Fedder [11] for the position tracking of probe-based magnetic disk drives. They added a constant controller gain that ensured a minimum phase margin of 60° to a linearized model of the actuator and experimentally stabilized the actuator up to 60% of the gap. Liu *et al* [18] used a lumped mass model for the cantilever beam to study the probe response and reported chaotic oscillation in the presence of forced excitations. The cantilever beam mode shapes were then used and a comprehensive study of the nonlinear system dynamics was carried out by Towfighian *et al* [19] to investigate the controller parameters for stable and bi-stable behavior, and chaotic oscillations.

The largest quasi-static micro-actuation range reported so far is limited to 60% of the capacitor gap for closed-loop actuators and 30% of the gap for open-loop actuators. Parallel-plate electrostatic actuators able to traverse the entire capacitor gap with reasonable actuation voltage are an important addition to the state-of-the-art since they will open the doors to wide spread use of these high-energy density actuators. For this purpose, we develop a large-stroke actuator by applying
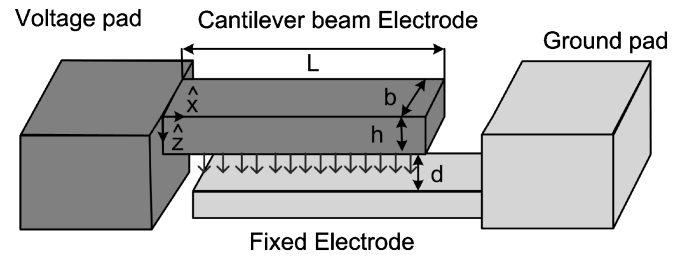

Figure 1. Schematic of the micro-beam oscillator.

a simplified control law to a micro-cantilever beam. We study the quasi-static and dynamic response of the large-stroke actuator experimentally and numerically to characterize its performance. In the following sections, we describe the closed-loop actuator model and report the numerical and experimental performance of the actuator in quasi-static and dynamic actuation modes, respectively.

2. Actuator model

The actuator consists of a polysilicon cantilever beam as a moving electrode above a fixed electrode (figure 1). A picture of the fabricated PolyMUMPS actuator is shown in figure 2. A feedback control system is added to the open-loop electrostatic actuator to extend the stable electrostatic actuation range.

The controller regulates the actuator voltage, and therefore the electrostatic force, to obtain a larger range of motion. A schematic of the closed-loop system is shown in figure 3. In this figure, V_{in} is the input voltage, V_c is the controller output voltage, G is a voltage gain and $\hat{w}$ is the deflection of the beam in the $\hat{z}$ direction (figure 1). The voltage applied between the two electrodes (see figure 3) creates the electrostatic forcing on the cantilever beam,

$$F_e \propto G^2 \frac{(V_{in} - V_c)^2}{(d - \hat{w})^2},\qquad(1)$$

where $d - \hat{w}$ is the gap.

The equation of motion of the closed loop is [19]

$$\rho A \frac{\partial^2 \hat{w}(\hat{x}, \hat{t})}{\partial \hat{t}^2} + EI \frac{\partial^4 \hat{w}(\hat{x}, \hat{t})}{\partial \hat{x}^4}$$
$$+ c \frac{\partial \hat{w}(\hat{x}, \hat{t})}{\partial \hat{t}} = \frac{\varepsilon_0 b G^2 (V_{in} - V_c)^2}{2(d - \hat{w}(\hat{x}, \hat{t}))^2}\qquad(2)$$

where A is the cross-sectional area of the beam, EI is the flexural rigidity of the beam and the coefficient c accounts for damping losses due to the beam motion through the air. Other system parameters are identified experimentally as described in Towfighian *et al* [20] and are given in table 1. To generalize the equation of motion, we use the following non-dimensional variables to rewrite equation (2):

$$x = \frac{\hat{x}}{L}, \qquad w = \frac{\hat{w}}{d}, \qquad t = \frac{\hat{t}}{T}\qquad(3)$$

where the time constant T is

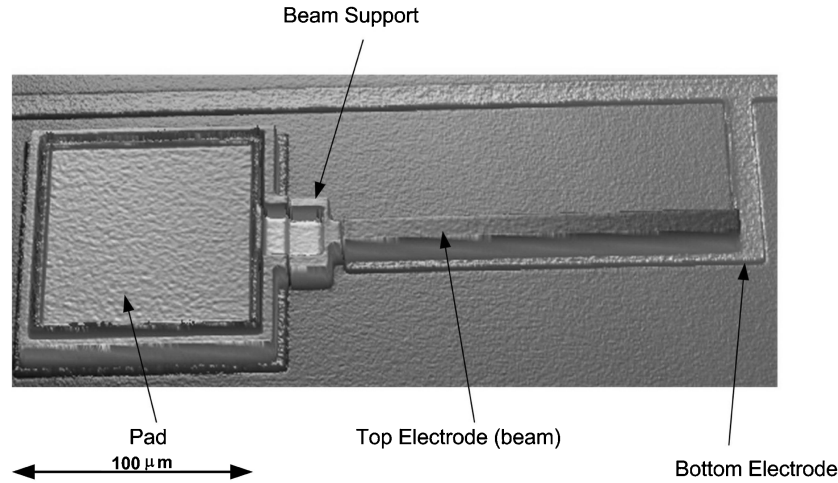$$T = \sqrt{\frac{\rho A L^4}{EI}}.\qquad(4)$$

Figure 2. A white-light image of the electrostatic actuator obtained with a WYKO NT1100 optical profiler.
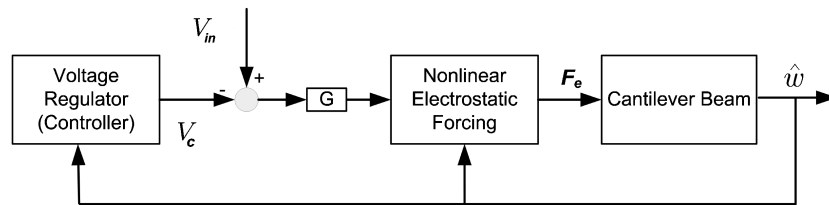

Figure 3. Closed-loop system.

We multiply the result by the denominator of the electrostatic force term to obtain

$$\ddot{w}(1-w)^2 + w^{(4)}(1-w)^2 + \mu\dot{w}(1-w)^2 = G^2\alpha(V_{\text{in}} - V_c)^2,$$

(5)

where

$$\mu = \frac{cL^4}{EIT}, \qquad \alpha = \frac{\varepsilon_0 bL^4}{2EId^3},$$

(6)

and $w^{(4)}$ is the fourth derivative of deflection with respect to the axial coordinate x. To transform equation (5) to an ordinary differential equation, it is discretized using separation of variables and Galerkin's method with the trial function chosen as the first mode shape of the cantilever beam. The set of ordinary differential equations of the actuator including the controller equation is then

$$\begin{cases} (\ddot{q} + \mu\dot{q} + \omega_1^2 q)(1 + c_1 q + c_2 q^2) = c_3 G^2\alpha(V_{\text{in}} - V_c)^2 \\ \dot{V}_c = -r\left(V_c - \frac{q}{1-q}\Psi\right) \end{cases}$$

(7)

where q is the beam tip deflection normalized with respect to the initial gap, over-dot means differentiation with respect to time, ω_1 is the first natural frequency of the beam and c_1, c_2 and c_3 are found by applying Galerkin's method. The parameters appearing in the differential equation for the controller voltage (V_c) [18] are the voltage gain G, displacement gain Ψ and controller damping r.

Typically in applications such as AFM-based memory devices or in programmable optical filters [3], actuators travel from an undeflected position to a static hold at a

Table 1. Actuator parameters.

| Parameter	Symbol	Value
Displacement gain	Ψ	0.5 V
Voltage gain	G	4.8
Controller damping	r	100
Density of polysilicon	ρ	2331 kg m^{-3}
Beam length	L	131 μm
Beam width	b	20 μm
Beam thickness	h	1.9 μm
Initial gap	d	1.9 μm
Non-dimensional damping coefficient	μ	0.157
Permittivity of air	ε	8.85 × 10^{-12} F m^{-1}
Modulus of elasticity	E	150 GPa

target location. In these applications, resonant and high-frequency oscillations are not advantageous. Henceforth, choosing an excitation frequency around one-fourteenth of the resonant frequency, large stable actuations are investigated quasi-statically. Restricting the tests to low frequency allows simplification of the control circuit. The controller equation (7) can be rewritten in the Laplace domain as

$$sV_c = -rV_c + r\Psi\frac{q}{1-q}$$

(8)

and after rearranging, this becomes

$$\frac{V_c}{\Psi\frac{q}{1-q}} = \frac{1}{1 + \frac{s}{r}}.$$

(9)

The righthand side of equation (9) is a low-pass filter with a non-dimensional cut-off frequency of r. When operating at non-dimensional frequencies much lower than the cut-off
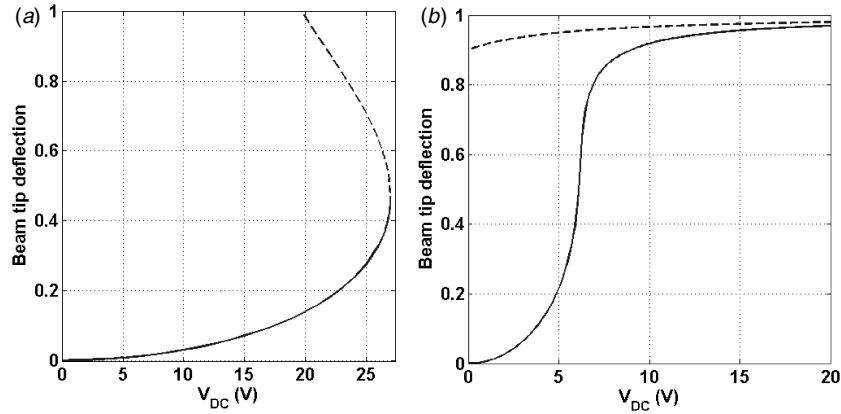
Figure 4. (*a*) Open-loop displacement, (*b*) closed-loop displacement. The dashed lines show the location of unstable equilibrium points (saddles) and the solid lines show the stable equilibrium location.

frequency $\hat{\Omega} \ll r$ (or dimensional frequencies $\Omega \ll r/T$), the ratio $\frac{s}{r}$ in equation (9) approaches zero and thus it can be simplified to

$$V_c \approx \Psi \frac{q}{1-q}. \tag{10}$$

Using the previous equation to generate the control voltage simplifies the implementation of the controller and allows for a more compact device. The revised system equations are then obtained as

$$\begin{cases} \left(\ddot{q} + \mu\dot{q} + \omega_1^2 q\right)(1 + c_1 q + c_2 q^2) = c_3 \alpha G^2 (V_{\text{in}} - V_c)^2 \\ V_c = \dfrac{q}{1-q} \Psi. \end{cases} \tag{11}$$

The stable actuator is obtained by setting the voltage regulator parameters to obtain a stable equilibrium point for most of the gap distance [19], figure 4(*b*). The results in part (*b*) of the figure were obtained by numerically solving the algebraic equations obtained by equating the time derivatives in equation (11) to zero. In this figure, the solid line shows the location of the stable equilibrium point and the dashed line shows the location of the unstable saddle point. While the stable equilibrium point defines the rest position of the beam, the stable manifold of the saddle delineates the basin of safe oscillations around that equilibrium position. The static profile reveals that the controller displaces the saddle away from the stable equilibrium point; this is revealed by comparing to the open-loop static response (figure 4(*a*)). The increased distance of the saddle from the stable equilibrium point creates a larger basin for safe motions to evolve around the equilibrium point.

3. Quasi-static actuation

3.1. Closed-loop system

The closed-loop system is implemented by introducing a circuit that acts as a voltage regulator. The controller function, the second of equations (11), was implemented using analog electronics [21]. Despite the advantages of digital control such as easy code changes, an analog system is chosen because of its fast response. A challenge with analog systems though is the difficulty in changing the controller function. The voltage
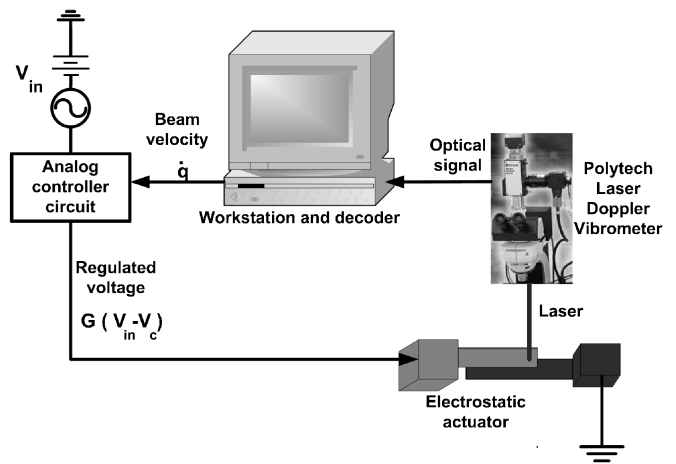
Figure 5. Schematic of the closed-loop system.

regulator input was provided by a signal function generator, and the regulator op-amps were operated using two power supplies. The intermediate parameters were measured along the circuit and were displayed on the oscilloscope.

A schematic of the closed-loop system is shown in figure 5 and further details can be found in [22]. First, the beam tip velocity $\dot{q}$ is measured with the vibrometer, the corresponding signal is then passed through a high-pass filter, cut off at 30 Hz, to eliminate ground vibration generated by the vacuum pump used to hold the chip in place. Next, the filtered velocity signal is integrated in the circuit to find the beam tip displacement q. The displacement signal is scaled so that the entire electrostatic gap is equivalent to 1 V. Next, the displacement signal is subtracted from a constant voltage of 1 to evaluate $(1 - q)$, and division is performed to find $\frac{q}{1-q}$. The result is multiplied by the displacement gain Ψ to find the control voltage V_c (equation (10)). This is subtracted from the input voltage V_{in}, and the result is finally multiplied by the voltage gain G to generate the regulated voltage $G(V_{\text{in}} - V_c)$. The regulated voltage is applied to the actuator. This voltage can control the beam position in the stable regime to create a stable large-stroke actuator. The schematic of the control circuit is shown in figure 6, where subtraction and multiplication
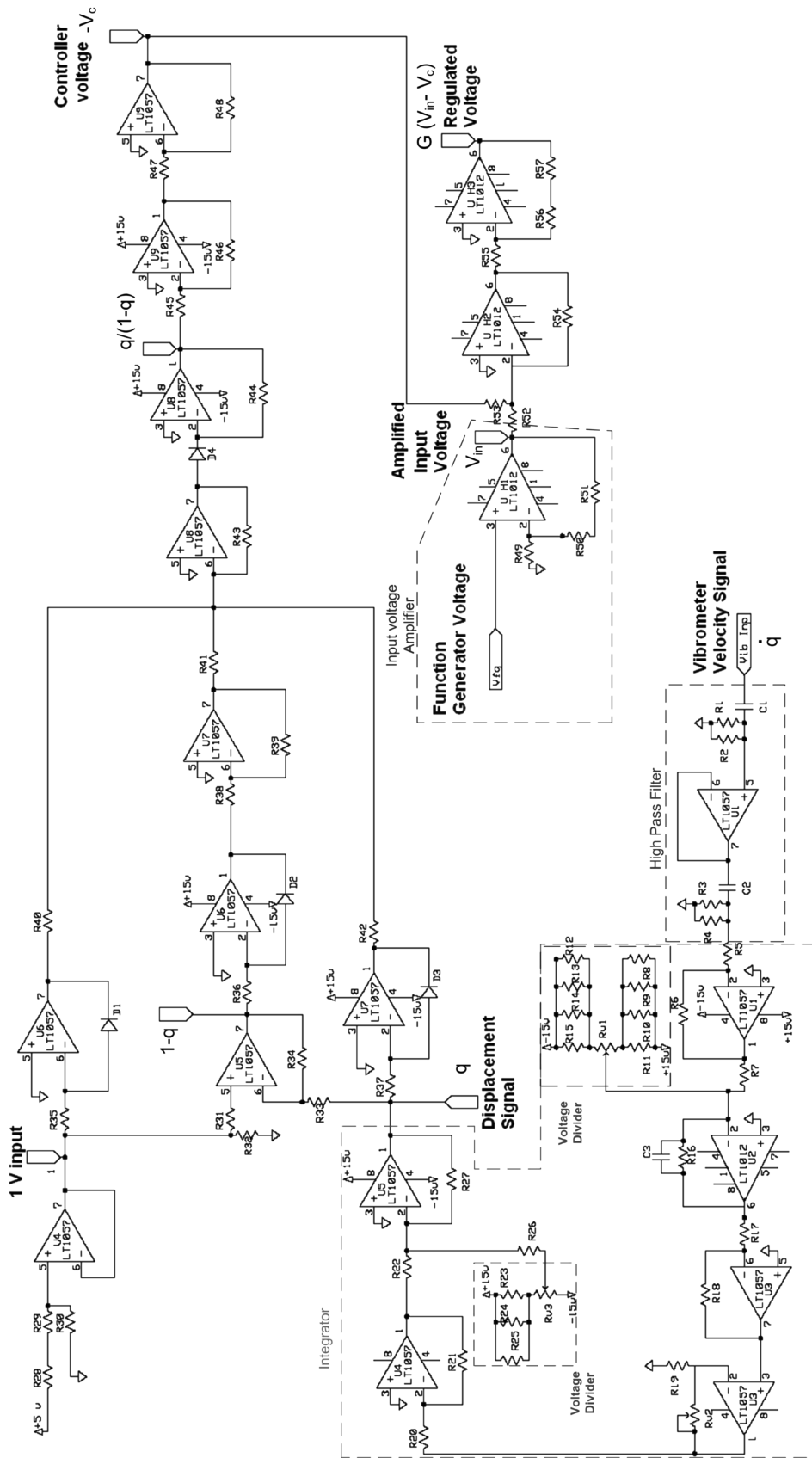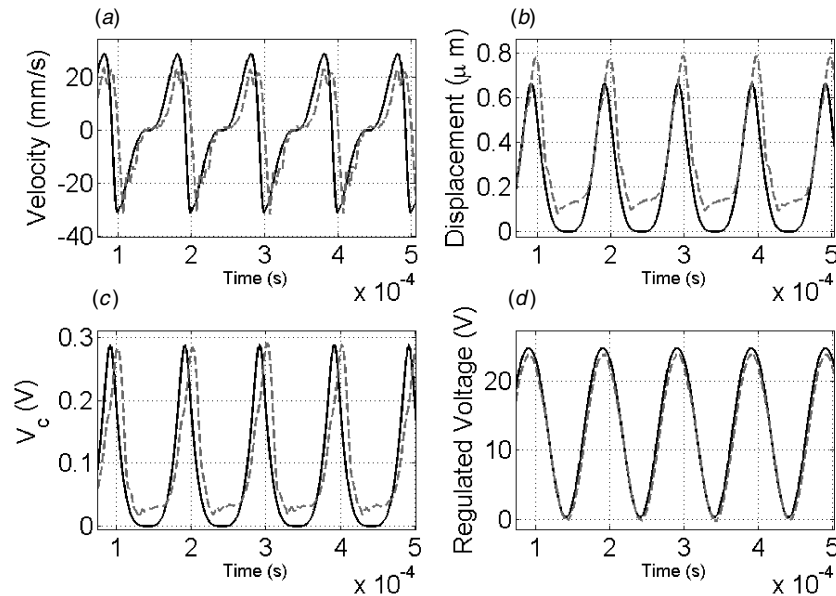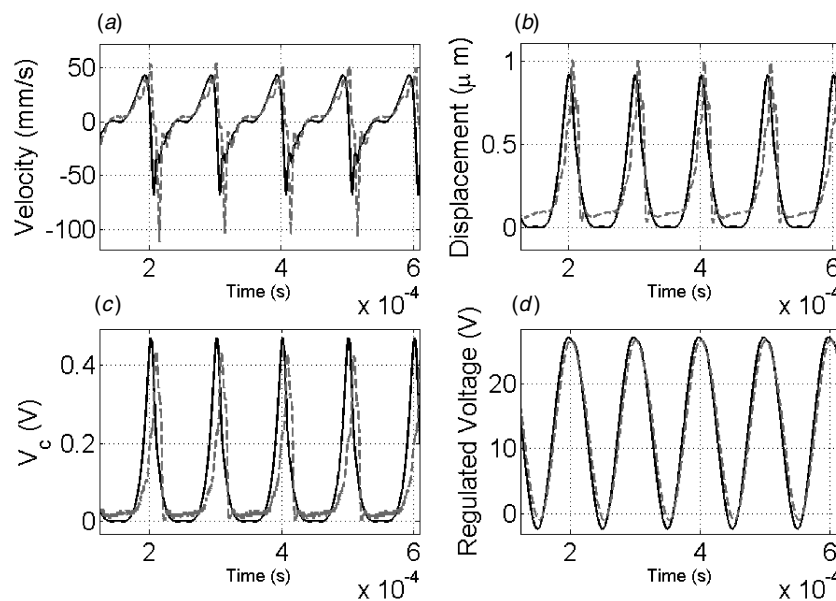
4

Figure 6. Schematic of the low-frequency controller circuit.

Figure 7. Closed-loop response to excitation at $v = 2.7$ V, $\omega = 10$ kHz. $----$ measured, ——— simulated. (*a*) Beam tip velocity, (*b*) beam tip displacement, peak at 37%, (*c*) controller voltage V_c, (*d*) regulated voltage $G(V_{in} - V_c)$. (Capacitor gap is 1.82 μm.)
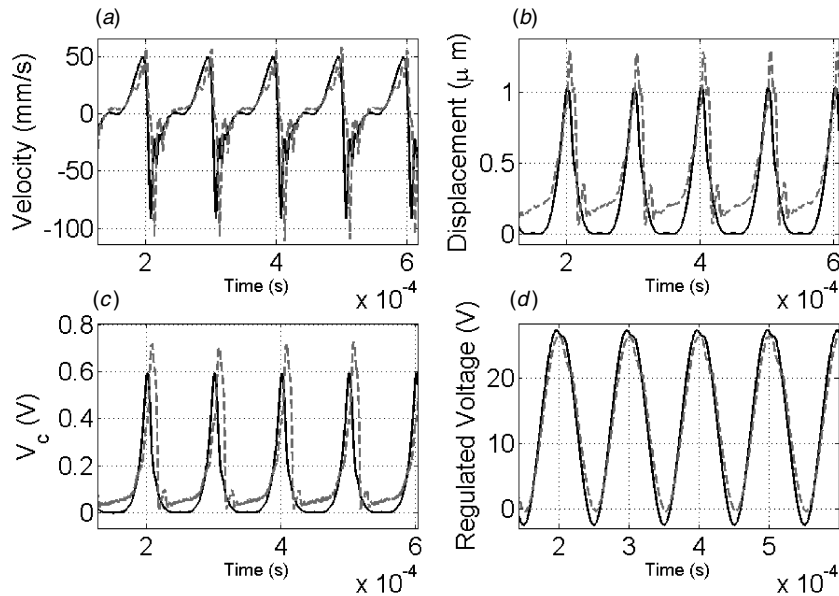

Figure 8. Closed-loop response to excitation at $v = 2.88$ V, $\omega = 10$ kHz. $----$ measured, ——— simulated. (*a*) Beam tip velocity, (*b*) beam tip displacement, peak at 52%, (*c*) controller voltage V_c, (*d*) regulated voltage $G(V_{in} - V_c)$. (Capacitor gap is 1.9 μm.)

are implemented using op-amps and division is realized using diodes [21].

The closed-loop actuator was tested using a sinusoidal excitation voltage according to $V_{in} = v(1 + \cos(\Omega t))$ that varies between zero and a maximum voltage that corresponds to a desired static location in figure 4(*b*). The maximum excitation, $2v$, corresponds to the horizontal axis of figure 4, and the target location corresponds to the vertical axis. Figures 7–11 compare experimental and simulated dynamic responses revealing quasi-static actuation with target positions located at 37%, 52%, 67%, 78% and 90% of the gap, respectively. Simulations were performed by numerically solving equation (11) using the beam parameters and the

damping ratio in table 1 identified in [20]. The frequency of excitation was set to 10 kHz. In comparison to the beam natural frequency of 140 kHz, the forced motion was quasi-static. The damping ratio was 0.157, the pull-in voltage was 25 V, and the beam length, width and thickness were 131, 20 and 1.9 μm, respectively. The gap distance was perturbed around the nominal value so that the magnitude of the maximum velocity obtained in simulations was equal to that obtained experimentally. Using this method, the capacitor gap was identified as $d = 1.82$ and 1.9 μ m for the beams employed in the tests shown in figures 7 and 8–11, respectively.

The experimental results in part (*a*) of the figures present the velocity of the actuator tip measured by the vibrometer

Figure 9. Closed-loop response to excitation at $v = 2.92$ V, $\omega = 10$ kHz. $----$ measured, —— simulated. (*a*) Beam tip velocity, (*b*) beam tip displacement, peak at 67%, (*c*) controller voltage V_c, (*d*) regulated voltage $G(V_{in} - V_c)$. (Capacitor gap is 1.9 μm.)
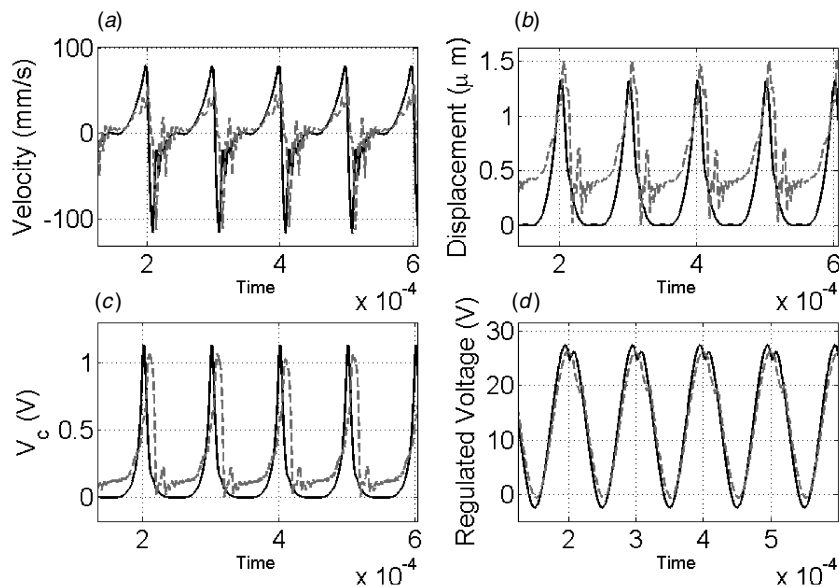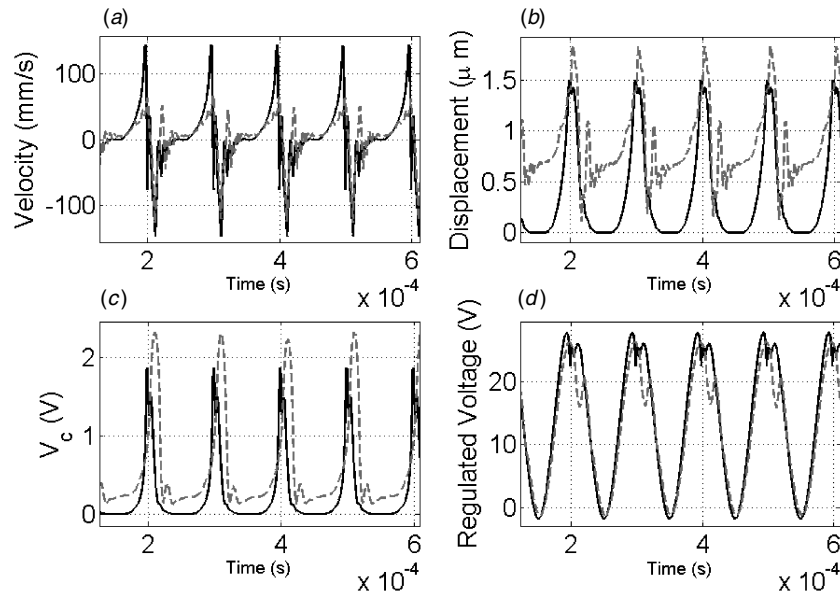

Figure 10. Closed-loop response to excitation at $v = 3$ V, $\omega = 10$ kHz. $----$ measured, —— simulated. (*a*) Beam tip velocity, (*b*) beam tip displacement, peak at 78%, (*c*) controller voltage V_c, (*d*) regulated voltage $G(V_{in} - V_c)$. (Capacitor gap is 1.9 μm.)

and part (*b*) represents the displacement found from the integration of the velocity signal in the circuit. Parts (*c*) and (*d*) show the measured controller voltage V_c and the regulated voltage applied to the actuator $G(V_{in} - V_c)$, respectively. The experimental results in parts (*a*) and (*b*) of the figures are filtered in MATLAB by local regression using weighted linear least squares and a first degree polynomial model that assigns lower weight to outliers in the regression. The method assigns zero weight to data outside six mean absolute deviations.

Good agreement between simulation and measured responses is observed for a broad range of actuation voltage. The smallest range is presented in figure 7, where though the controller voltage does not exceed 0.3 V and the regulated voltage does not go beyond the open-loop pull-in voltage of

25 V, the actuator traverses a trajectory that spans to 0.67 μm or 37% of the gap which is greater than the 33% stability limit for open-loop systems. The low signal to noise ratio for small displacements prevents the controlled motions from tracking the trajectory in the troughs. However, as the displacement increases and the signal to noise ratio improves, the controller follows the desired trajectory well.

Keeping the excitation frequency constant at 10 kHz and increasing the peak voltage from 2.88 to 3.2 V for a beam with a larger gap of 1.9 μm, the travel ranges increase from 52% (0.94 μm) to 90% (1.73 μm) in figures 8–11. This increase corresponds to a controller voltage rise from 0.45 to 2.2 V as shown in part (*c*) of these figures and to the

Figure 11. Closed-loop response to excitation at $v = 3.2$ V, $\omega = 10$ kHz. $----$ measured, —— simulated. (*a*) Beam tip velocity, (*b*) beam tip displacement, peak at 90%, (*c*) controller voltage V_c, (*d*) regulated voltage $G(V_{in} - V_c)$. (Capacitor gap is 1.9 μm.)

changes in the regulated voltage shape in part (*d*). The qualitative change in the regulated voltage originates from the increase of the controller voltage V_c in part (*c*) as the beam displacement reaches its maximum in part (*b*). Because the controller voltage peak and the input voltage peak have the same phase, there is a voltage drop at the peak of the regulated voltage across the capacitor $G(V_{in} - V_c)$ shown in figure 11(*d*). The voltage drop at the peak of the regulated voltage plays an important role in stabilizing the actuator. As the actuation voltage increases in the open-loop actuator, the electrostatic force increases causing more deflection in the beam which rapidly increases the electrostatic force even more. This positive feedback loop drives open-loop actuators to pull-in. The voltage regulator, on the other hand, interrupts this process by dropping the voltage and the electrostatic force as the displacement increases helping to balance it with the mechanical spring force and making large displacements feasible. At the maximum displacement, the actuator reverses direction in part (*a*) as the mechanical force dominates the electrostatic force and the beam returns to the undeflected position. It is noted that the signal to noise ratio in parts (*a*) and (*b*) deteriorates as the input voltage increases, though that affects the oscillation that takes place around the undeflected position and not around the target large displacement points.

The beam tip comes to within 400 and 100 nm of the substrate surface for the trajectories shown in figures 10 and 11, respectively. This proximity is desirable for reading and writing in probe-based high-capacity data storage devices [11] using miniaturized AFM arrays.

Observing the displacement profiles, it is apparent that more oscillations occur as the actuator reverses its direction of motion away from the higher peaks and into the trough. These oscillations modulate the displacement and velocity profiles with oscillations at the natural frequency of the beam ω_1. They occur because of the sudden motion reversal at the peak. On the other hand, the oscillations are not present at the counter motion reversal as the actuator climbs out of the trough because of our choice of input signal which guarantees a trough wide enough for the initial oscillations to die out and a gradual motion reversal.

The modulated oscillations are not seen in the predicted path as the model uses a linear viscous damping term to represent the dissipation mechanisms in the actuator. In averaging out the highly nonlinear effects of squeeze-film damping, it overestimates the amount of damping present for the small oscillations in the trough around the undeflected position. The effects of the discrepancy between the linear damping model and the actual nonlinear damping effect are also clear in the simulated velocity matching the minimum measured negative velocity but not the maximum positive velocity in figures 10 and 11. This difference between the simulated and measured velocities grows as the actuation range increases. These limitations notwithstanding, the actuator reaches its target at the peak with minimal delay. Further, unlike the leveraged bending method, the regulated voltage does not exceed 27 V, slightly larger than the pull-in voltage of 25 V.

At the peak voltage drop, a small phase difference can be seen between the simulations and experiments in figures 10(*d*) and 11(*d*) that is caused by the delays imposed by the op-amps in the controller circuit. The phase difference magnitudes are 8.6° and 7.5°, respectively, in those figures. This phase shift can be minimized using more precise non-inverting op-amps. However, actuation ranges are not affected by the controller phase delay.

The ultimate positions reached at different peak voltages are summarized in figure 12 as well as the static deflection versus voltage curves shown earlier in figure 4(*b*). Figure 12 reveals a good agreement between the static simulation results and the quasi-static experimental measurements, thereby
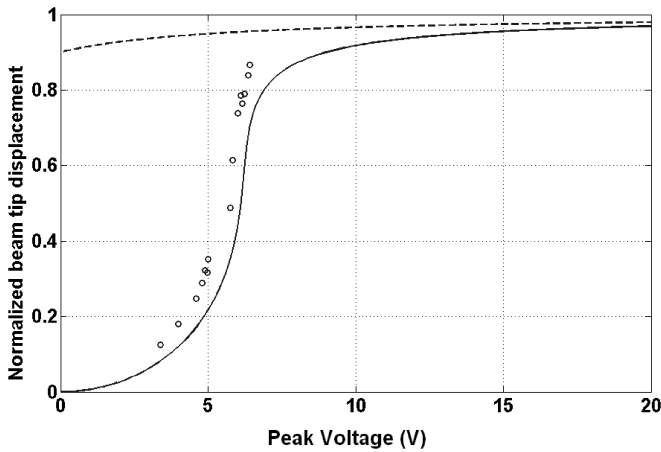
Figure 12. Peak actuator displacement versus peak voltage (2*v*). − − − simulated unstable equilibrium points, —— simulated stable equilibrium points, ○ experimental results. (Capacitor gap is 1.9 μm.)

justifying the basic assumption underlying the simplified controller development.

3.2. Virtual regulator

Examining the response of the actuator to the controlled voltage, we postulated that applying the regulated voltage waveform obtained from the simulation directly to the beam without using the analog regulator could lead to similar results. The experimental setup consisted exclusively of the micro-beam, a signal generator and a vibrometer to measure the beam tip velocity and an analog integrator. Simulations were performed using the closed-loop control model to generate the regulated voltage signal. The signal generator was then used to produce the customized waveform, the beam response was

measured using the vibrometer and the velocity was integrated using the analog integrator to find the beam displacement. The results are depicted in figure 13, where the customized voltage signal is shown in part (*c*). Exciting the beam with the proposed waveform eliminates the need for the external feedback circuit while allowing for an actuation range as large as 75% of the gap which is significantly larger than the traditional open-loop limit of 33% of the gap. Under this paradigm, the controller can be constructed as an off-line filter that can be used to filter out the components of the command voltage that drive the pull-in instability.

4. Dynamic actuation

### 4.1. Closed-loop superharmonic resonances

The closed-loop actuator can also act as a resonator in regions of the frequency spectrum where superharmonic resonances appear. Exciting the system at one frequency, the system is responding at multiple frequencies. We studied the superharmonic resonances available at low-frequency excitations (<22 kHz). The results are presented in figure 14 showing, on the left, the fast Fourier transform (FFT) of 2^{12} velocity data points and, on the right, the phase portrait obtained from plotting the measured velocity versus the integrated displacement. The beam under test has nominal dimensions of $175 \times 10 \times 2$ with a gap of 2 μm and a natural frequency of 80 kHz. All experiments were conducted on the same day to eliminate variation in the plant parameters due to aging and changes in temperature and humidity. The superharmonic resonances are verified by the FFT, where a train of FFT peaks extending from the excitation frequency to the natural frequency exists and the number of peaks reveals the order of the superharmonic resonance. The superharmonic resonances of order 8, 6 and 5 are reported at excitation
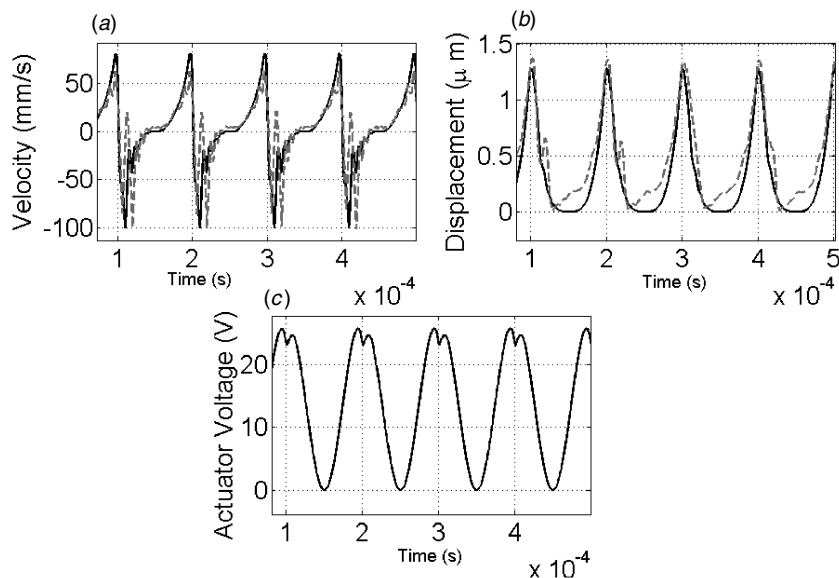
Figure 13. Actuator open-loop response to a customized input waveform. − − − − measured, —— simulated response to excitation at $v = 3$ V, $\omega = 10$ kHz for a beam with the dimensions of 131 μm × 20 μm × 1.9 μm with the gap of 1.82 μm, and the controller parameters of $\Psi = 0.5$ V, $G = 4.8$.
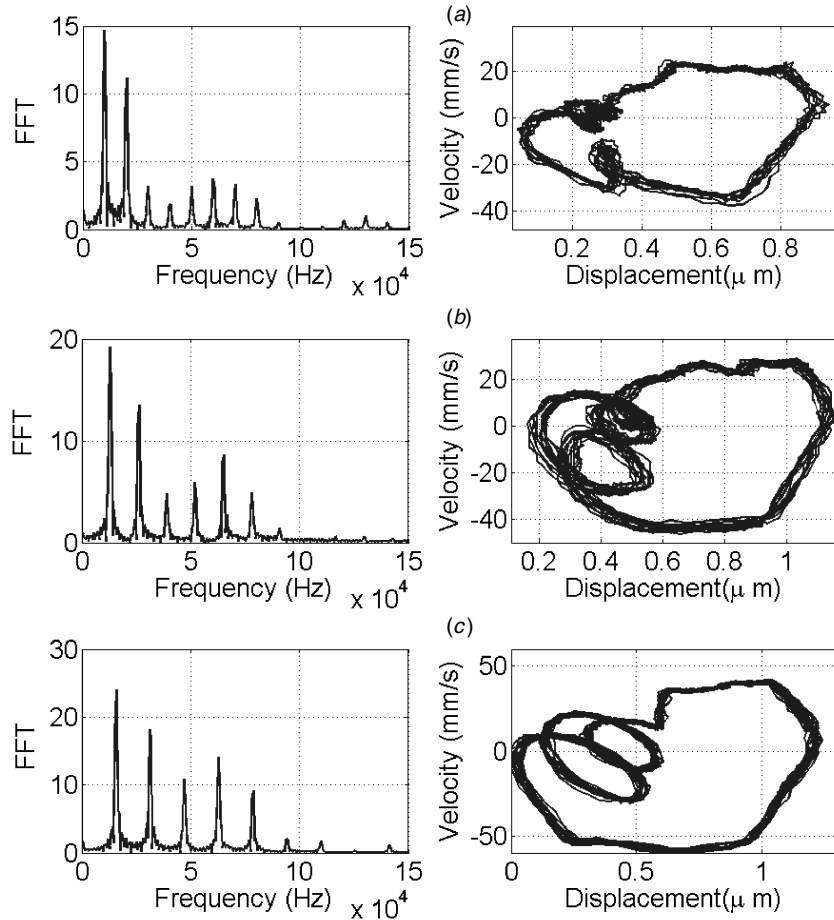
Figure 14. FFT of the tip velocity and phase portrait for a beam with a natural frequency of 80 kHz obtained when the controller parameters are $G = 2$, $\Psi = 0.5$ V, and the excitation amplitude is $v = 3.56$ V for the superharmonic resonances of (*a*) order 8 at $\omega = 10$ kHz, (*b*) order 6 at $\omega = 13$ kHz and (*c*) order 5 at the excitation $\omega = 15.7$ kHz.
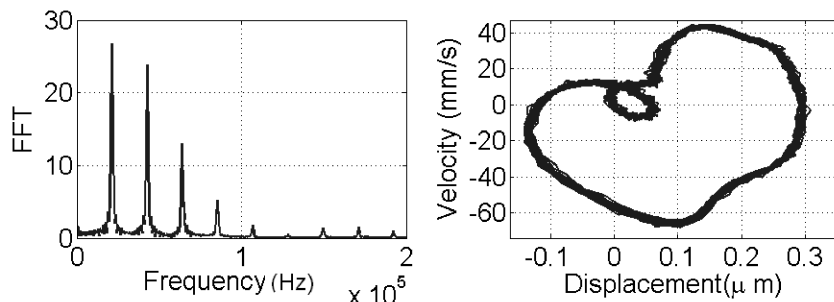

Figure 15. FFT of the tip velocity and phase portrait for the superharmonic resonance of order 4 obtained for a beam with a natural frequency of 85 kHz when the controller parameters are $G = 2$, $\Psi = 0.5$ V at the excitation $v = 2.78$ V, $\omega = 21.36$ kHz.

frequencies of 10, 13 and 15.7 kHz, respectively, with the same voltage excitation magnitudes $v = 3.56$ V. The superharmonic orbits shown expand along the displacement and velocity axes as the order of the superharmonic drops from 8 to 5. The stretching of the orbit along the displacement axis corresponds to higher dynamic amplification of the input at lower orders of the superharmonic resonance that leads to a higher signal to noise ratio.

Testing a similar beam with a natural frequency of 85 kHz, the superharmonic resonance of order 4 was observed as shown in figure 15 at an excitation frequency of

21.36 kHz. Although the excitation voltage is lower than the previous set of tests, the phase portrait shows an orbit comparable with the previous three cases of superharmonic resonance. As the order of superharmonic resonances drops, the regularity increases and fewer harmonics appear in the FFT resulting in the reduction of the number of loops in the phase portrait. Although superharmonic resonances of orders 1/2 and 2 have been reported by Younis *et al* [23], the first instance of higher order resonances in MEMS electrostatic actuators is observed here.
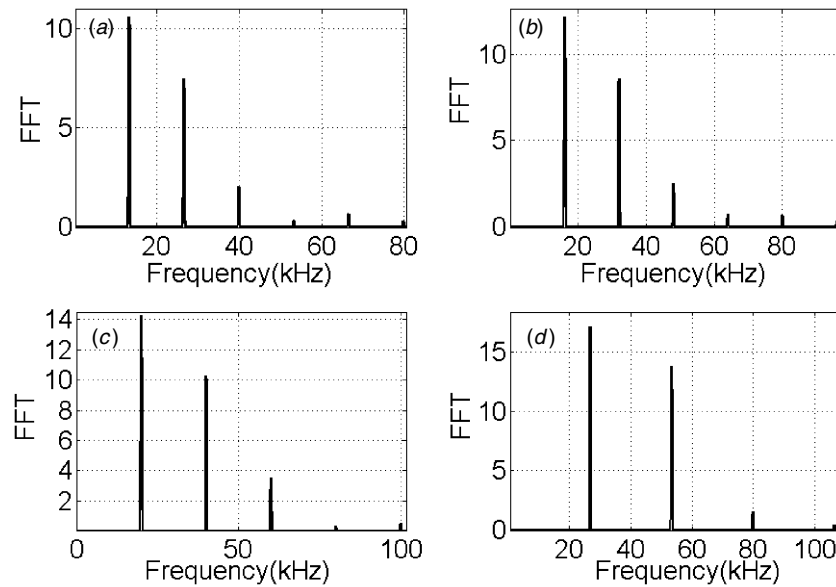
Figure 16. The superharmonic resonances of an actuator with the nominal dimensions of 175 μm $\times$ 10 μm $\times$ 2 μm and a gap of 2 μm (*a*) order 6 obtained at $V_{DC} = 5.2$ V, $V_{AC} = 4.7$ V, $\Omega = 13.3$ kHz, (*b*) order 5 obtained at $V_{DC} = 5.2$ V, $V_{AC} = 4.16$ V, $\Omega = 16$ kHz, (*c*) order 4 obtained at $V_{DC} = 5.2$ V, $V_{AC} = 3.88$ V, $\Omega = 20$ kHz, (*d*) order 3 obtained at $V_{DC} = 5.2$ V, $V_{AC} = 3.32$ V, $\Omega = 26.6$ kHz.

4.2. Open-loop superharmonic resonances

Superharmonic resonance was also observed in the open-loop system for excitation at integer fractions of the natural frequency. The beam had the nominal dimensions of 175 $\times$ 10 $\times$ 2 and a gap of 2 μm with a natural frequency of 80 kHz. The dc voltage was held constant at 5 V. Figure 16 presents the FFT of the beam tip velocity response. Superharmonic resonances of order 6–3 in descending order are depicted in parts (*a*)–(*d*) of this figure. The orders of the superharmonics are clear from the number of peaks in the FFT up to and including the natural frequency peak at 80 kHz.

Although open-loop superharmonic resonances require less equipment to produce the resonance, the closed-loop superharmonics carry comparatively more power in higher harmonics as indicated by the FFT peaks for superharmonic orders of 6, 5 and 4. The larger kinetic energy of the higher harmonics makes closed-loop superharmonic resonances good candidates for applications such as secure communication devices [24], where sending and receiving a signal in a wide range of frequencies rather than a single frequency are desirable.

5. Conclusion

The actuation range of a closed-loop parallel-plate electrostatic actuator in attracting mode was extended in quasi-static operation mode to 90% of the capacitor gap. This is a significant improvement since the largest reported quasi-static stroke does not exceed 60% of the gap [11]. The actuator consists of a micro-cantilever beam and a voltage controller developed for low-frequency applications such as trajectory tracking and micro-positioning. The closed-loop actuator voltage requirements are moderate; in fact, the total actuation voltage is about the pull-in voltage of the open-loop actuator.

Likewise, the travel range of the open-loop actuator was increased using a customized voltage waveform generated using a model of the closed-loop system. Exciting the beam with the proposed waveform eliminates the need for an external feedback system while allowing for actuation in quasi-static operation mode with a stroke as large as 75% of the gap. Such a large stroke in an open-loop actuator is well beyond the present restricted quasi-static actuation range of one-third of the gap. Our results show that this longstanding limitation can be overcome with the careful analysis and design of open- and closed-loop actuators.

In the closed-loop actuator, the tip velocity is measured using a laser Doppler vibrometer and the corresponding voltage signal is used to regulate the actuator voltage. For practical deployment of the actuator, the vibrometer can be replaced by a piezoresistor implanted at the root of the micro-beam to act as a displacement sensor. The actuator is then combined with the analog controller on a CMOS chip. It could be emphasized that both our open- and closed-loop actuators were tested successfully in an open air environment with significant external disturbances and without any requirements for a vacuum chamber.

Higher order superharmonic resonances were also observed for the first time both for open-loop and closed-loop electrostatic actuators. The superharmonic resonances are important observations in nonlinear MEM systems and can be used to develop sensors and communication receivers.

References

[1] Borovic B, Hong C, Liu A Q, Xie L and Lewis F L 2004 Control of a MEMS optical switch *43rd IEEE Conf. on Decision and Control (CDC) (Nassau, Bahamas)* vol 3 pp 3039–44

[2] Sugihwo F, Larson M C and Harris J S 1998 Micromachined widely tunable vertical cavity laser diodes *J. Microelectromech. Syst.* **7** 48–55

[3] Hung E S 1998 Positioning, control, and dynamics of electrostatic actuators for use in optical and RF systems *PhD Thesis* Massachusetts Institute of Technology

[4] Chung S 1999 Design and fabrication of 10 × 10 micro-spatial light modulator array for phase and amplitude modulation *Sensors Actuators* A **78** 63–70

[5] Vettiger P *et al* 2002 The 'millipede'—nanotechnology entering data storage *IEEE Trans. Nanotechnol.* **1** 39–55

[6] Seeger J I and Boser B E 2003 Charge control of parallel-plate, electrostatic actuators and the tip-in instability *J. Microelectromech. Syst.* **12** 656–71

[7] Maithripala D H S, Berg J M and Dayawansa W P 2005 Control of an electrostatic microelectromechanical system using static and dynamic output feedback *Trans. ASME J. Dyn. Syst.* **127** 443–50

[8] Guardia R, Dehe A, Aigner R and Castaner L M 2002 Current drive methods to extend the range of travel of electrostatic microactuators beyond the voltage pull-in point *J. Microelectromech. Syst.* **11** 255–63

[9] Chan E K and Dutton R W 2000 Electrostatic micromechanical actuator with extended range of travel *J. Microelectromech. Syst.* **9** 321–8

[10] Hung E S and Senturia S D 1999 Extending the travel range of analog-tuned electrostatic actuators *J. Microelectromech. Syst.* **8** 497–505

[11] Lu M S-C and Fedder G K 2004 Position control of parallel-plate microactuators for probe-based data storage *J. Microelectromech. Syst.* **13** 759–69

[12] Chen J, Weingartner W, Azarov A and Giles R C 2004 Tilt-angle stabilization of electrostatically actuated micromechanical mirrors beyond the pull-in point *J. Microelectromech. Syst.* **13** 988–97

[13] Agudelo C G, Packirisamy M, Zhu G and Saydy L 2009 Nonlinear control of an electrostatic micromirror beyond pull-in with experimental validation *J. Microelectromech. Syst.* **18** 914–23

[14] Zhao Y, Francis E H T, Siong F C and Zhou G 2006 Stabilization of dual-axis micromirrors beyond the pull-in point by integral sliding mode control *J. Micromech. Microeng.* **16** 1242–50

[15] Piyabongkarn D, Sun Y, Rajamani R, Sezen A and Nelson B J 2005 Travel range extension of a MEMS electrostatic microactuator *IEEE Trans. Control Syst. Technol.* **13** 138–45

[16] Owusu K O and Lewis F L 2007 Solving the 'pull-in' instability problem of electrostatic microactuators using nonlinear control techniques *2nd IEEE Int. Conf. on Nano/Micro Engineered and Molecular Systems (Bangkok, Thailand)* pp 1190–5

[17] Nikpanah M, Wang Y, Lewis F and Liu A 2008 Real time controller design to solve the pull-in instability of MEMS actuator *10th Int. Conf. on Control, Automation, Robotics and Vision (Hanoi, Vietnam)* pp 1724–9

[18] Liu S, Davidson A and Lin Q 2004 Simulation studies on nonlinear dynamics and chaos in a MEMS cantilever control system *J. Micromech. Microeng.* **14** 1064–73

[19] Towfighian S, Heppler G R and Abdel-Rahman E M 2011 Analysis of a chaotic electrostatic micro-oscillator *J. Comput. Nonlinear Dyn.* **6** 011001

[20] Towfighian S, Seleim A, Abdel-Rahman E M and Heppler G R 2010 Experimental validation for an extended stability electrostatic actuator *Proc. ASME 2010 Int. Design Engineering Technical Conf. (Montreal, QC, Canada)* DETC2010-28983

[21] Seleim A 2010 Design and implementation of a controller for an electrostatic MEMS actuator and sensor *Master's Thesis* University of Waterloo

[22] Towfighian S 2010 A large-stroke electrostatic micro-actuator *PhD Thesis* University of Waterloo

[23] Younis M I and Alsaleem F 2009 Exploration of new concepts for mass detection in electrostatically-actuated structures based on nonlinear phenomena *J. Comput. Nonlinear Dyn.* **4** 021010

[24] Wang Y C, Adams S G, Thorp J S, MacDonald N C, Hartwell P and Bertsch F 1998 Chaos in MEMS, parameter estimation and its potential application *IEEE Trans. Circuits Syst.* **45** 1013–20